Chapter 9

Proton structure in QCD

Literature:

- Halzen/Martin [1], Chap. 8-10.

This chapter reviews the study of the proton structure, which lasted form after World War II to the closure of HERA (DESY) in 2007. The understanding gained from those results is of essential importance to predict cross-sections for the Tevatron (Fermilab) and the LHC (CERN), since both of them use hadrons as colliding particles.

First, the methods used to study the proton structure are presented and the relevant kinematic quantities are defined, starting from the similar case of $e^-\mu^-$-scattering. We then generalize to the case of a composite hadron. After that, the Bjorken scaling is introduced. Finally, the steps leading to the discovery of the uncharged parton – the gluon – are described.

One must remember that the link between the particle zoo and the results concerning the proton structure was not at all obvious, as the quark model had not yet imposed itself as a leading theory.

9.1 Probing a charge distribution & form factors

To probe a charge distribution in a target one can scatter electrons on it and measure their angular distribution (Fig. 9.1). The measurement of the cross-section can be compared with the expectation for a point charge distribution,

$$\frac{d\sigma}{d\Omega} = \left(\frac{d\sigma}{d\Omega}\right)_{\text{point}} |F(q)|^2, \tag{9.1}$$

where $F(q)$ is called the **form factor**, and $q := k_i - k_f$ is the momentum transfer from the probing particle to the target. The momentum transfer is also related to the resolution power of the probe.

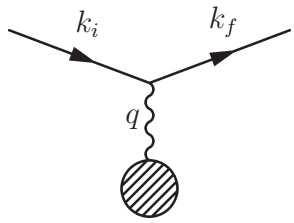

Figure 9.1: Probing a charge distribution

When probing a point ($\equiv$ spinless & structureless) target, $F(q) \equiv 1$ and one gets the **Mott cross section**,

$$\left(\frac{d\sigma}{d\Omega}\right)_{\text{point}} = \frac{(Z\alpha)^2 E^2}{4k^4 \sin^4(\theta/2)} \left(1 - \frac{k^2}{E^2}\sin^2(\theta/2)\right), \tag{9.2}$$

where Z is the electric charge measured in units of the elementary charge, E and $k = |k_i| = |k_f|$ are respectively the energy and the momentum of the probing particle, and θ is the scattering angle. One typically measures θ and E of the scattered electron.

Comparing the angular dependence of the differential cross-section of eletrons scattering off protons with the Mott cross sections, measurements show that the two distributions do not agree at large scattering angles as shown in Fig. 9.2.

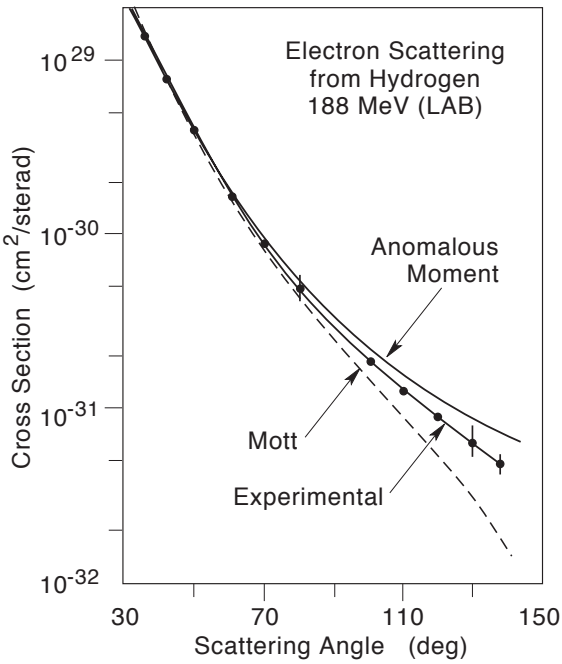

Figure 9.2: Mott cross section (dashed line) and compared to the experimental data form electron-hydrogen scattering. The measurement disagrees with the point-linke cross section at large scattering angles.

9.2 Structure functions

Starting from the example of scattering of two different elementary spin-$\frac{1}{2}$ particles, an ansatz is made for the general case.

9.2.1 $e^-\mu^-$-scattering in the laboratory frame

In the case of the $e^-\mu^-$-scattering in the laboratory frame at high energy ($s \gg M = m_\mu$), the matrix element is given by,

$$\begin{aligned}\overline{|\mathcal{M}_{fi}|^2} &= \frac{e^4}{q^4} L^{\mu\nu}_{e^-} L^{\mu^-}_{\mu\nu} \\ &= \frac{8e^4}{q^4} 2M^2 E' E \left(\cos^2(\theta/2) - \frac{q^2}{2M^2} \sin^2(\theta/2) \right),\end{aligned}$$

where E' is the energy of the scattered electron, and the transferred momentum,

$$q^2 \approx -2k \cdot k' \approx -4EE' \sin^2(\theta/2),$$

yielding – upon inclusion of the flux factor and phase space – the differential cross section for $e^-\mu^-$ in the laboratory frame,

$$\frac{d\sigma}{d\Omega} = \frac{\alpha^2}{4E^2 \sin^4(\theta/2)} \frac{E}{E'} \left(\cos^2(\theta/2) - \frac{q^2}{2M^2} \sin^2(\theta/2) \right). \tag{9.3}$$

9.2.2 e^-p-scattering & the hadronic tensor

When dealing with hadrons, the possibility of inelastic scattering, i.e. scattering where the final state contains excited states or other particles than the probe and the scattering particle, must be taken into account, shown in the Feynman diagram,

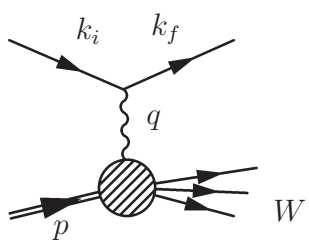

where W is the invariant mass of the particles in the final state (Sect. 4.4.4, p. 51). The scattering cross-section as a function of W is shown in Fig. 9.3. One notes the elastic peak at $W = m_p$ followed by a peak at 1232 MeV corresponding to the Δ^+ resonance and produced by the reaction,

$$e^-p \to e^-\Delta^+ \to e^-p\pi^0$$

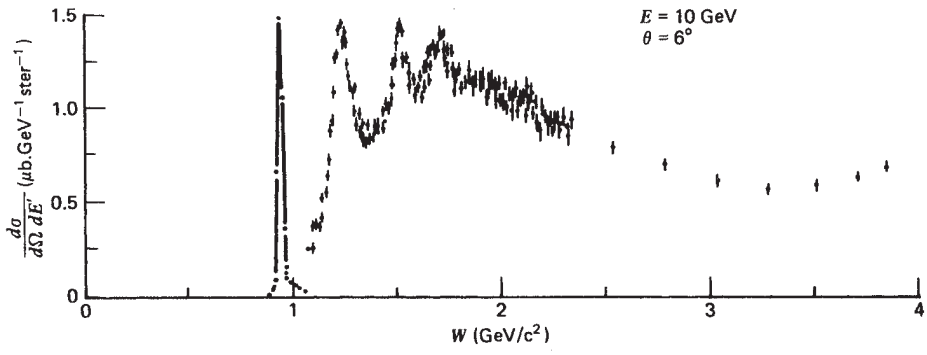

Figure 9.3: Differential cross section as a function of the invariant mass W.

To calculate the e^-p-scattering, one makes the substitution $L^{\mu\nu}_{\mu^-} \to W^{\mu\nu}_p$, where,

$$W^{\mu\nu}_p = -W_1 g^{\mu\nu} + \frac{W_2}{M^2} p^\mu p^\nu + \frac{W_4}{M^2} q^\mu q^\nu + \frac{W_5}{M^2}(p^\mu q^\nu + q^\mu p^\nu), \tag{9.4}$$

is the most general rank-2 tensor with functions $W_1, ..., W_5$ constructed from Lorentz scalars[1] depending on the internal structure of the proton, constructible from the 4-momentum of the proton (p) and the momentum transfer (q).

Imposing current conservation $\partial_\mu j^\mu_p = 0$, one can rewrite W_4 and W_5 in terms of W_1 and W_2 :

$$W_5 = -\frac{p \cdot q}{q^2} W_2$$
$$W_4 = \left(\frac{p \cdot q}{q^2}\right)^2 W_2 + \frac{M^2}{q^2} W_1,$$

Replacing W_4 and W_5 in Eq. (9.4) :

$$W^{\mu\nu}_p = W_1 \left(-g^{\mu\nu} + \frac{q^\mu q^\nu}{q^2}\right) + \frac{W_2}{M^2}\left(p^\mu - \frac{p \cdot q}{q^2} q^\mu\right)\left(p^\nu - \frac{p \cdot q}{q^2} q^\nu\right). \tag{9.5}$$

W_1 and W_2 are the so-called the **structure functions** of the proton. They depend on two independent variables,

$Q^2 := -q^2$: the 4-momentum transfer squared,

$\nu = \dfrac{p \cdot q}{M}$: the energy transferred to the nucleon by the scattering electron,

[1]The "missing" W_3-term is related to the axial part of the current, and is relevant when considering the weak interaction. It is discarded in what follows.

or their dimensionless counterparts,

$$x = -\frac{q^2}{2p \cdot q} = \frac{Q^2}{2M\nu} \text{ : the Bjorken scaling } x\text{-variable,} \qquad 0 \leq x \leq 1,$$
$$y = \frac{p \cdot q}{p \cdot k_i}, \qquad 0 \leq y \leq 1.$$

With the variables defined above, we have the following expression for the invariant mass :

$$W^2 = (p+q)^2 = M^2 + 2M\nu - Q^2. \tag{9.6}$$

The elastic scattering case $W^2 = M^2$ corresponds to the value $x = 1$. Fig. 9.4 shows the

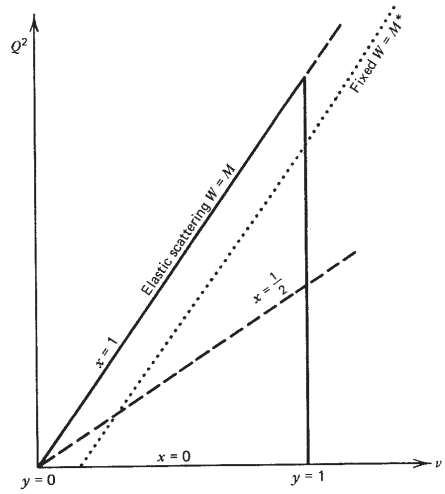

Figure 9.4: Allowed kinematical region of the Q^2-ν-plane.

kinematic region in the Q^2-ν-plane.

Using the hadron tensor, Eq. (9.5), the scattering matrix element is,

$$L^{e^-}_{\mu\nu} W^{\mu\nu}_p = 4EE' \left(W_2(Q^2,\nu)\cos^2(\theta/2) + W_1(Q^2,\nu)\sin^2(\theta/2) \right)$$

Including the flux and phase-space factors (Sect. 2.2.4, p. 13 & 3.2.3, p. 23) one finds the differential cross-section in the laboratory frame,

$$\frac{d\sigma}{dE' d\Omega} = \frac{\alpha^2}{4E^2 \sin^4(\theta/2)} \left(W_2(Q^2,\nu)\cos^2(\theta/2) + W_1(Q^2,\nu)\sin^2(\theta/2) \right)$$

Integrating over the energy of the outgoing election E', one gets,

$$\frac{d\sigma}{d\Omega} = \frac{\alpha^2}{4E^2 \sin^4(\theta/2)} \frac{E'}{E} \left(W_2(Q^2,\nu)\cos^2(\theta/2) + W_1(Q^2,\nu)\sin^2(\theta/2) \right).$$

9.3 Parton model

The key factor for investigating the proton substructure is the wavelength of the probing photon, which is related to the transferred momentum by,

$$\lambda \sim \frac{1}{\sqrt{Q^2}},$$

Therefore, large momentum transfer is equivalent to high resolution. As shown in Fig. 9.5, for $\lambda \approx 1\,\text{fm}$, one can "see" the proton as a single particle, whereas for, $\lambda \ll 1\,\text{fm}$, the

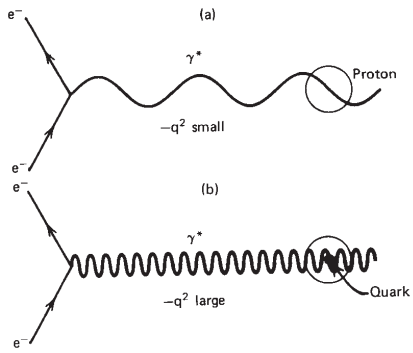

Figure 9.5: Relationship between resolution and transferred momentum.

probed particles are the constituents of the proton.

9.3.1 Bjorken scaling

J. Bjorken proposed in 1968 that, in the limit of infinite Q^2, the structure functions should only depend on the scaling variable x, and not on Q^2 and ν independently. This corresponds to postulating that at large Q^2 the inelastic e^-p-scattering is a sum of elastic scatterings of the electron on free **partons** within the proton, as illustrated below.

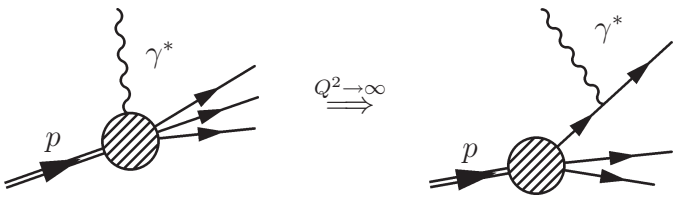

In this limit, one defines then the functions,

$$F_1(x) := \lim_{Q^2\to\infty} MW_1(Q^2,\nu), \tag{9.7}$$

$$F_2(x) := \lim_{Q^2\to\infty} \nu W_2(Q^2,\nu). \tag{9.8}$$

9.3.2 SLAC-MIT experiment

To test the hypothesis of Bjorken, a joint experiment of the SLAC and MIT groups was performed at the SLAC laboratory. Sketches and photographs of the experiment are shown in Fig. 9.6.

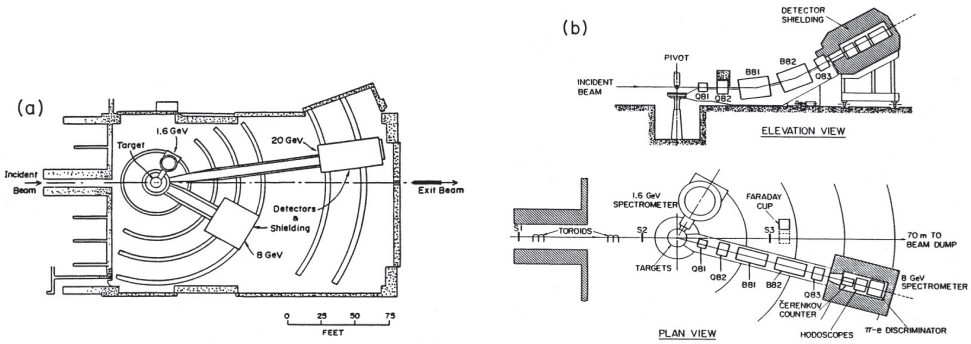

(a) (b)

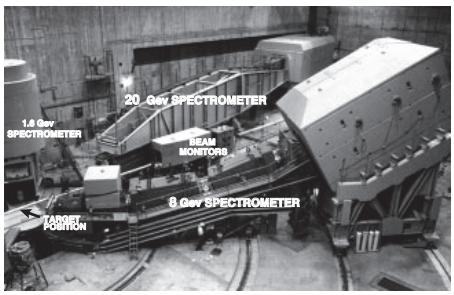

(c)

Figure 9.6: *SLAC-MIT experiment.* (a), (b) Sketches showing the 1.5 GeV, 8 GeV and 20 GeV spectrometers. (c) Photograph of the experiment.

The setup measured the scattering cross-section for fixed energies of the scattered electron and various angles. Fixing x (or $\omega = \frac{1}{x}$) one gets different values of Q^2 by varying the angle. The experimental result is shown in Fig. 9.7. This experiment confirmed the scaling hypothesis of Bjorken and gave a decisive piece of evidence in favour of the parton model introduced by Feynman in 1969. This model describes the proton as composed of **partons** which are the object one "sees" during an e^-p-scattering. One may describe the scattering process as shown in the following diagrams,

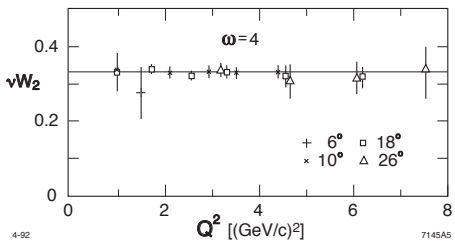

Figure 9.7: Experimental evidence for Bjorken scaling as measured at the SLAC-MIT experiment ($\omega = 1/x$).

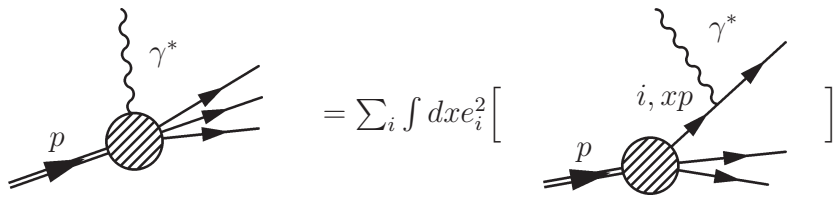

The sum runs over all possible partons, each carrying an electric charge e_i (in units of the elementary charge) and a fraction x of the total momentum of the proton. This gives us a physical interpretation of the Bjorken scaling variable x. Since the fraction of proton momentum carried by the i-th parton is not known a priori, one needs to integrate over all possible values of x between zero (the parton carries no momentum) and one (the parton carries all the proton momentum).

The probability $f_i(x)$ that the struck parton carries a fraction x of the proton momentum is called **parton distribution function** (PDF). The total probability must be equal to 1, in order for the proton as a whole to carry all its momentum :

$$\sum_i \int_0^1 dx\, x f_i(x) = 1. \tag{9.9}$$

In Feynman's parton model the structure functions are sums of the parton densities constituting the proton,

$$\nu W_2(Q^2, \nu) \to F_2(x) = \sum_i e_i^2 x f_i(x) \tag{9.10}$$

$$M W_1(Q^2, \nu) \to F_1(x) = \frac{1}{2x} F_2(x) \tag{9.11}$$

9.3.3 Callan-Gross relation

The result,

$$\boxed{2xF_1 = F_2}, \tag{9.12}$$

is known as **Callan-Gross relation** and is a consequence of quarks being spin-$\frac{1}{2}$ particles. It can be derived by comparing the e^-p and $e^-\mu^-$ differential cross sections and setting the mass of the quark to be $m = xM$. Remembering the definitions of F_1 and F_2, Eqs. (9.7) and (9.8), one has,

$$\frac{F_1(x)}{F_2(x)} = \frac{W_1(Q^2,\nu)}{W_2(Q^2,\nu)}\frac{M}{\nu},$$

and since the scattering is elastic with a point particle (the parton),

$$\begin{aligned} 2W_1(Q^2,\nu) &= \frac{Q^2}{2m^2}\delta\left(\nu - \frac{Q^2}{2m}\right) \\ W_2(Q^2,\nu) &= \delta\left(\nu - \frac{Q^2}{2m}\right) \qquad \Rightarrow \frac{W_1(Q^2,\nu)}{W_2(Q^2,\nu)} = \frac{Q^2}{4m^2}, \end{aligned}$$

and one gets the desired result, by putting in the definition of x and $m = xM$,

$$\frac{F_1(x)}{F_2(x)} = \frac{Q^2}{4m^2}\frac{M}{\nu} = \frac{Q^2}{2M\nu}\frac{1}{2x^2} = \frac{1}{2x}$$

Fig. 9.8 shows the Q^2-independence of the Callan-Gross relation.

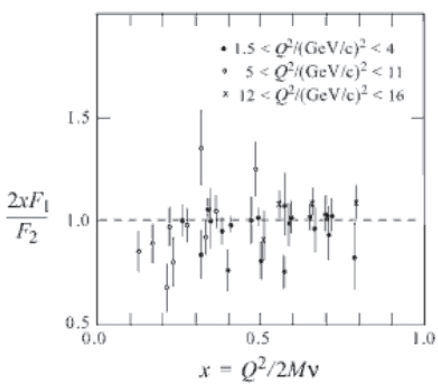

Figure 9.8: Experimental evidence for the Callan-Gross relation.

9.3.4 Parton density functions of protons and neutrons

The proton is know to be composed of two up and one down quarks (Sect. 7.3, p. 131). These quarks are known as valence quarks and are denoted q_v. They are the ones determining the properties of a hadron. It can however occur (in particular at high Q^2, corresponding to a high resolution) that a valence quark radiates a gluon which then splits in a quark-antiquark pair which is then probed by the virtual photon. These quarks are referred to as sea quarks and are denoted q_s.

In the case of e^-p-scattering and e^-n-scattering, writing q^N instead of $f_q^N(x)$ for convenience and using Eq. (9.10), we get respectively,

$$\frac{1}{x}F_2^{ep} = \left(\frac{2}{3}\right)^2 (u^p + \bar{u}^p) + \left(\frac{1}{3}\right)^2 (d^p + \bar{d}^p) + \left(\frac{1}{3}\right)^2 (s^p + \bar{s}^p) \tag{9.13}$$

$$\frac{1}{x}F_2^{en} = \left(\frac{2}{3}\right)^2 (u^n + \bar{u}^n) + \left(\frac{1}{3}\right)^2 (d^n + \bar{d}^n) + \left(\frac{1}{3}\right)^2 (s^n + \bar{s}^n), \tag{9.14}$$

where we have discarded the contributions of partons heavier than the strange quark.

One makes the assumption that these functions are not independent (exchanging an up quark for a down turns basically a proton into a neutron), and defines the total PDF of a given quark as the sum of its valence and sea components,

$$u := u_v + u_s = u^p = d^n$$
$$d := d_v + d_s = d^p = u^n.$$

Furthermore, we assume that the three lightest quark flavours (u,d,s) occur with equal probability in the sea:

$$S := u_s = \bar{u}_s = d_s = \bar{d}_s = s_s = \bar{s}_s.$$

Combining all definitions and assumptions one obtains,

$$\frac{1}{x}F_2^{ep} = \frac{1}{9}(4u_v + d_v) + \frac{4}{3}S \tag{9.15}$$

$$\frac{1}{x}F_2^{en} = \frac{1}{9}(4d_v + u_v) + \frac{4}{3}S. \tag{9.16}$$

At small momentum fractions ($x \approx 0$) the structure function is dominated by low-momentum $q\bar{q}$-pairs constituting the "sea", and hence

$$\frac{F_2^{en}}{F_2^{ep}} \to 1,$$

whereas for $x \approx 1$ the valence quarks dominate and,

$$\frac{F_2^{en}}{F_2^{ep}} \to \frac{1}{4}.$$

The experimental evidence is shown in Fig. 9.9.

Fig. 9.10 shows the distribution of F_2^{ep} that one would observe in different scenarios of proton structure.

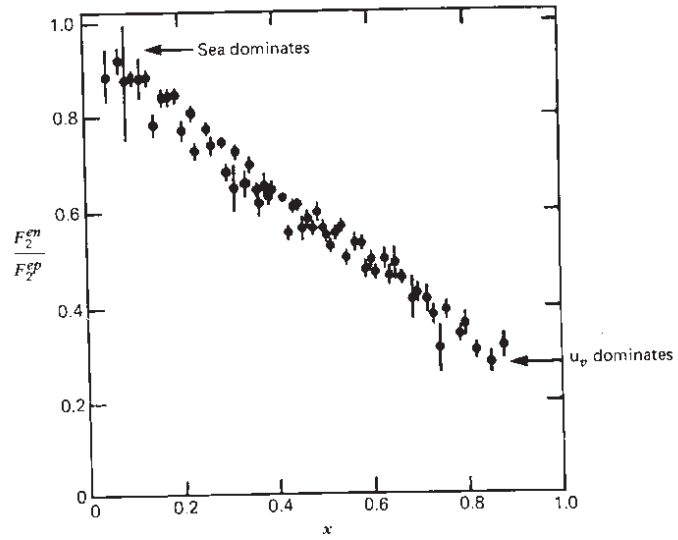

Figure 9.9: Ratio of the proton and neutron structure functions as a function of the Bjorken x-variable.

9.4 Gluons

9.4.1 Missing momentum

Summing the measured momenta of the partons cited above should give the proton momentum. However this is not the case.

$$\int_0^1 dx\ x(u + \bar{u} + d + \bar{d} + s + \bar{s}) = 1 - \varepsilon_g,$$

where,

$$\varepsilon_q := \int_0^1 dx\ x(q + \bar{q}).$$

The experimental data, neglecting the contribution of strange quarks, show that,

$$\int_0^1 dx F_2^{ep} = \frac{4}{9}\varepsilon_u + \frac{1}{9}\varepsilon_d = 0.18,$$

$$\int_0^1 dx F_2^{en} = \frac{1}{9}\varepsilon_u + \frac{4}{9}\varepsilon_d = 0.12.$$

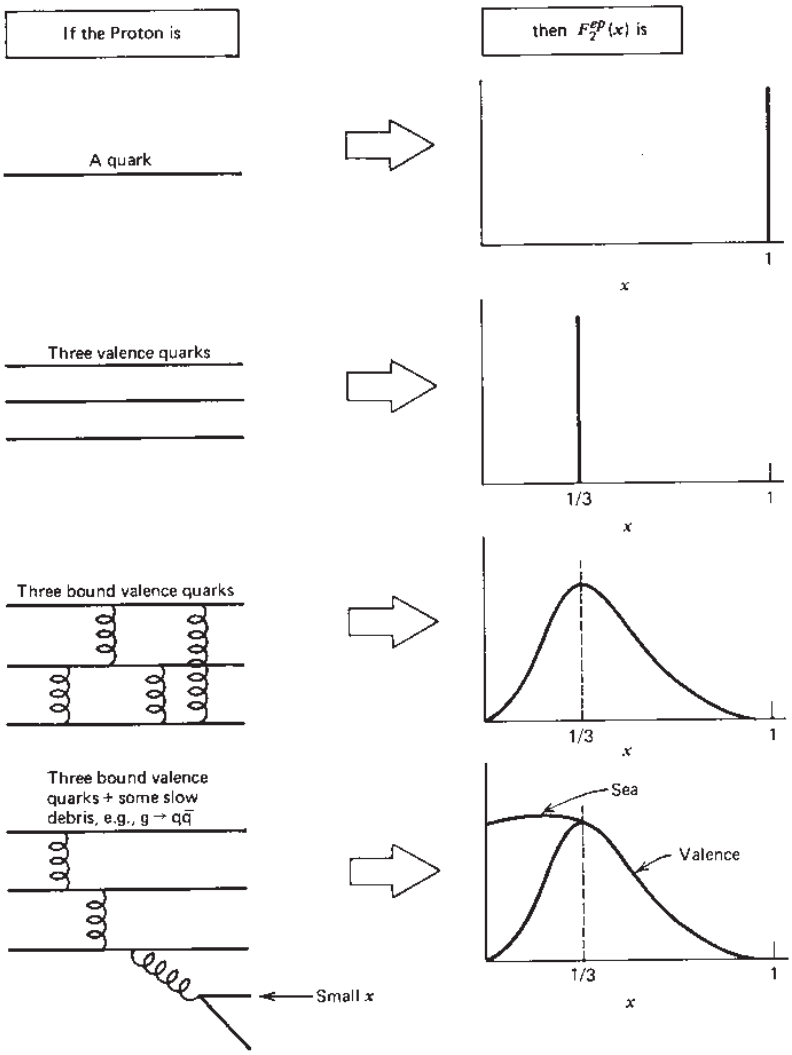

Figure 9.10: Structure functions F_2^{ep} in different scenarios of the proton structure.

Therefore,

$$\varepsilon_u = 0.36$$
$$\varepsilon_d = 0.18,$$

and the fraction of the proton momentum not carried by quarks is,

$$\varepsilon_g = 1 - \varepsilon_u - \varepsilon_d = 0.46.$$

Almost half of the proton momentum is carried by electrically uncharged partons. By repeating the scattering experiments with neutrinos instead of electrons, one observes that these uncharged partons do not interact weakly either. The parton carrying the missing momentum is now known as the **gluon**, the gauge boson of QCD.

9.4.2 Gluons and the parton model at $\mathcal{O}(\alpha\alpha_s)$

By including the gluons into the parton model, the following diagrams need to be taken into account :

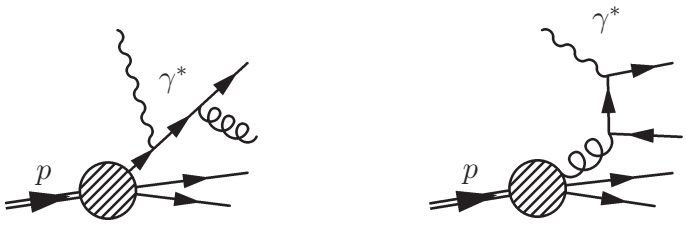

Looking specifically at the contribution of the first diagram, and using the kinematic variables defined in the following diagram,

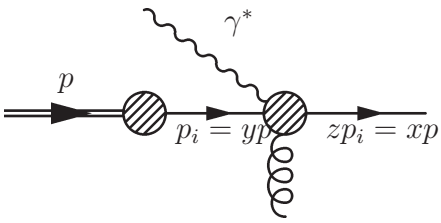

one can show that the contribution to the proton structure function is of the form :

$$\frac{1}{x}F_2^{\gamma^* q\to qg} = \sum_i e_i^2 \int_x^1 \frac{dy}{y} f_i(y) \left[\frac{\alpha_s}{2\pi} P_{qq}(x/y) \log\left(\frac{Q^2}{\mu^2}\right)\right], \tag{9.17}$$

where μ is a cutoff to regularize soft gluon emission and,

$$P_{qq}(z) = \frac{4}{3}\left(\frac{1+z^2}{1-z}\right),$$

is called splitting function. It is the probability of a quark to emit a gluon and reduce momentum by a fraction z. It is obviously divergent for soft gluons ($z \to 1$).

From the form of Eq. (9.17), one sees that Q^2 appear explicitely, and not divided by $2M\nu$. This logarithmic term is responsible for the phenomenon of scaling violations wo be discussed in the next chapter.

Why did the SLAC-MIT experiment not see this violation? The effect of scaling violation is only visible at extremely small x-values which were not available at this time. The scaling violation was indeed observed in later experiments as we will discuss in the following sections.

9.5 Experimental techniques

The main site dedicated to the study of the proton structure is the HERA accelerator (DESY), shown in Fig. 9.11. It was the only e^-p-collider ever built and reached the beam energies $E_e = 30\,\text{GeV}$ and $E_p = 900\,\text{GeV}$ for electrons and protons respectively.

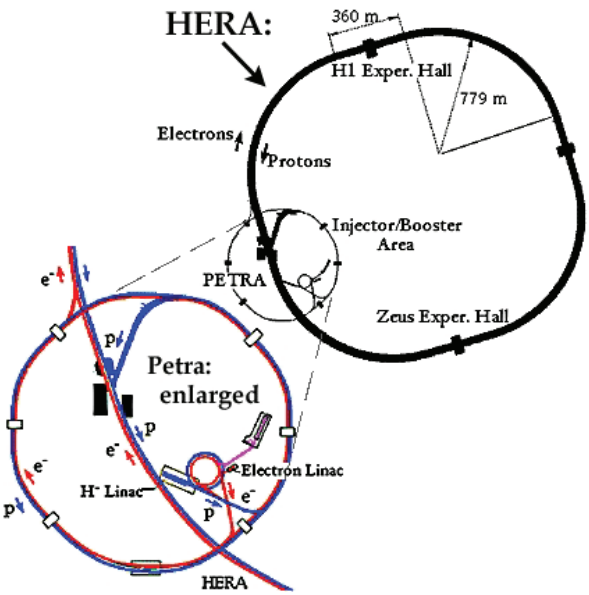

Figure 9.11: Schematics of the HERA accelerator at DESY.

Fig. 9.12 shows the coverage of the Q^2-x-kinematic region achieved at HERA and other experiments. The data at low Q^2 and low x allowed the observation of scaling violation and definitively confirmed the existence of the gluon as a constituent of the proton.

Fig. 9.13 shows the sketches of the H1 and ZEUS experiments at HERA, as well as the integrated luminosity collected by ZEUS. One can notice the asymmetrical configuration due to the different beam energies.

A typical deep inelastic scattering (DIS) event at ZEUS is shown in Fig. 9.14. One can observe the different properties of the final state : the quark jet deposits energy in the hadron calorimeter, while the electron is stopped in the electromagnetic section. The angles of the electron and hadronic system are measured in the central tracking chamber.

A "two jets" event, corresponding to the reaction,

$$e^- + p \to e^- + q + \bar{q} + X,$$

where X denotes the proton remnant (whose products are visible in the forward calorimeter), is shown in Fig. 9.15. An interesting feature of this event is the presence of a muon in correspondence of the jet. This muon may originate from the decay of a heavy quark.

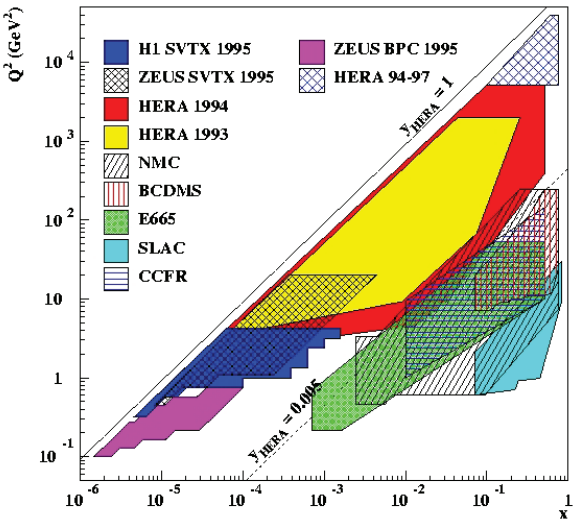

Figure 9.12: Coverage of the Q^2-x-kinematic region at HERA.

Since scaling is no longer preserved, both Q^2 and x (or $y = \frac{Q^2}{sx}$) have to be measured. Those can be obtained by measuring the energy E'_e and angle θ_e of the scattered eletron and using,

$$y_e = 1 - \frac{E'_e}{2E_e}(1 - \cos\theta_e)$$
$$Q_e^2 = 2E_e E'_e(1 + \cos\theta_e).$$

Fig. 9.16 shows the kinematic region measured at ZEUS while Fig. 9.17 shows the experimental results for the structure function F_2 as well as the NLO QCD fits. For low values of x, the scaling violation appears very clearly. It is due to the inclusion of the processes containing gluons.

Finally, Fig. 9.18 shows the measurement of the proton PDFs achieved at HERA. The relative importance of the sea and gluon distribution can be seen to vary significantly for Q^2 between $1.9\,\mathrm{GeV}^2$ and $10\,\mathrm{GeV}^2$ (note the scale reduction!). One can notice similarities with the expectation shown in Fig. 9.10.

9.6 Parton model revisited

In the following two sections we formalize the foregoing discussion and derive the expression of the QCD improved parton model for $F_2(x, Q^2)/x$ given in Eq. (9.17).

As we have seen the proton is a bound state of three quarks with strong binding. "Strong binding" says that the quark binding energy is much larger than the light quark masses: $E_{\text{bind}} \gg m_q$. Compare this to the weak binding of the hydrogen atom electron: $E_{\text{bind}} \ll m_e$.

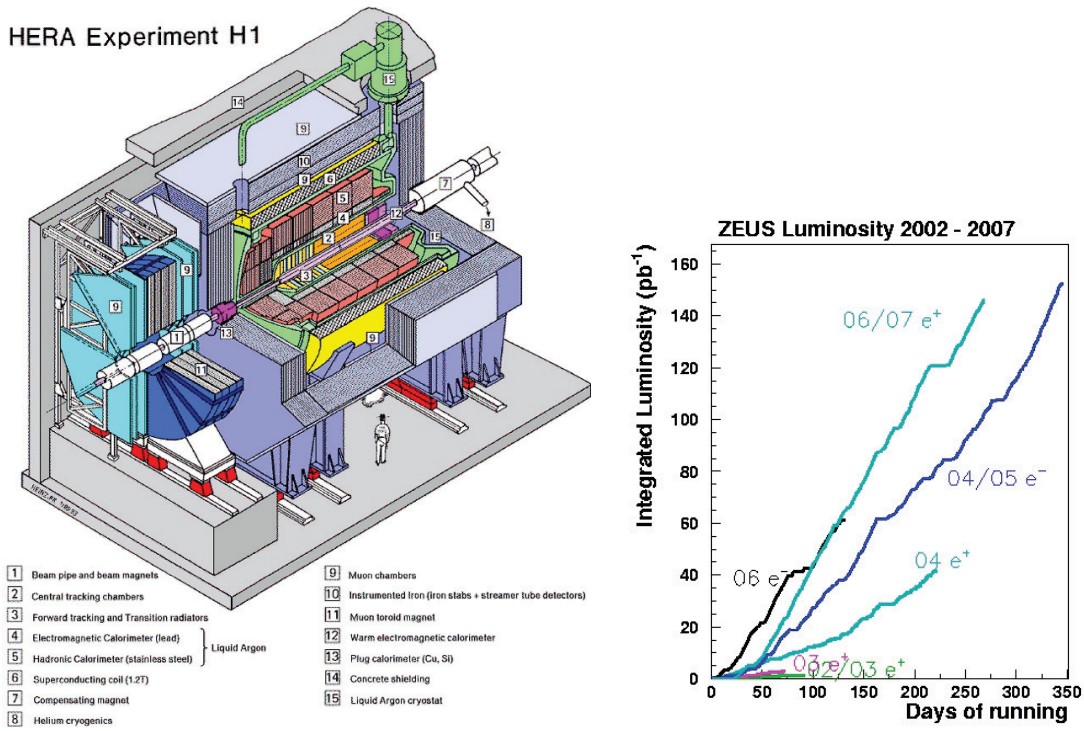

(a) (b)

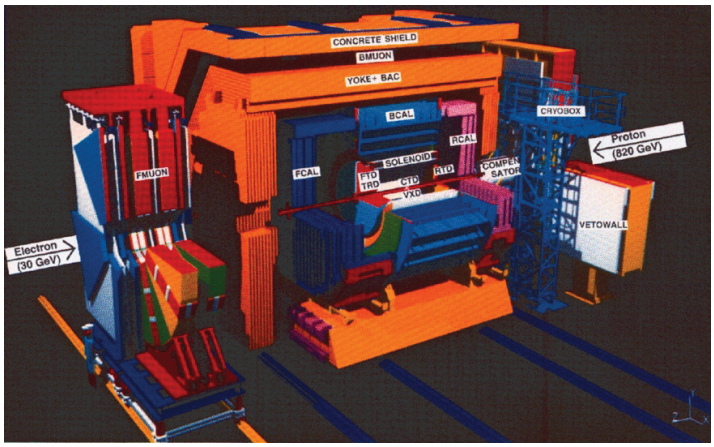

(c)

Figure 9.13: *Experiments at HERA*. (a) H1. (b) Luminosity integrated by the ZEUS during its operation. (c) ZEUS.

We consider a proton with large momentum ($|\vec{p}| \gg m_p$):

$$p^\mu = \begin{pmatrix} \sqrt{|\vec{p}|^2 + m_p^2} \\ \vec{p} \end{pmatrix} \simeq \begin{pmatrix} |\vec{p}| \\ \vec{p} \end{pmatrix}.$$

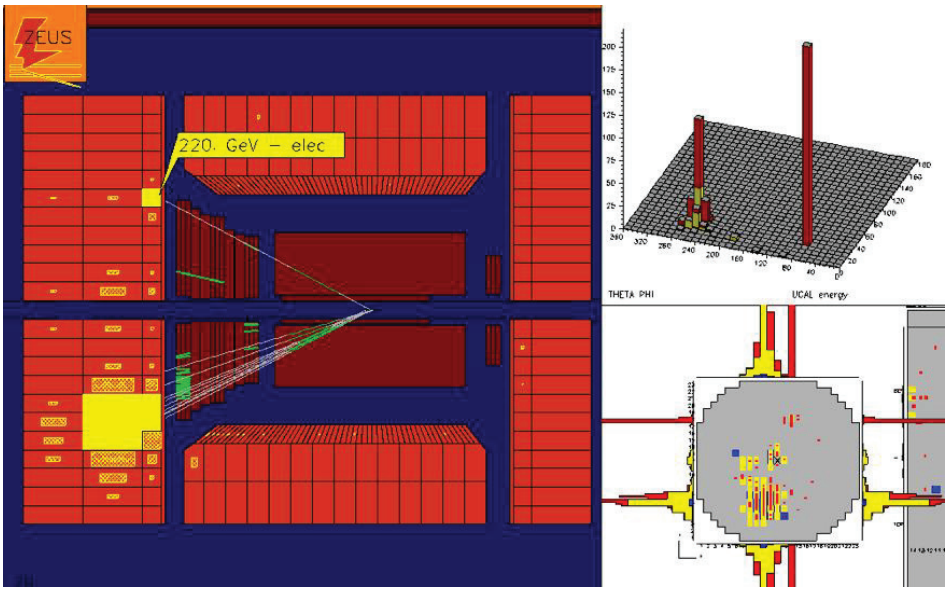

Figure 9.14: DIS event recorded by the ZEUS experiment.

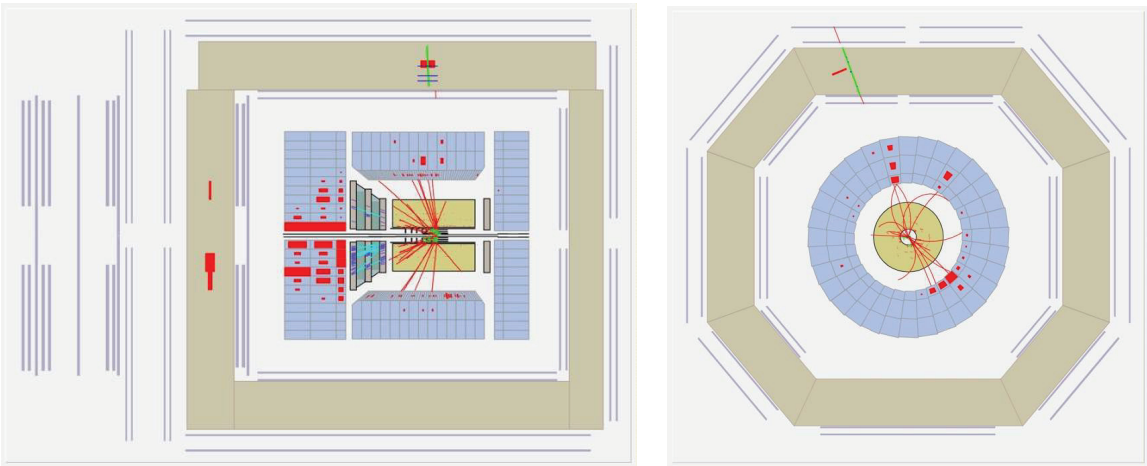

(a) (b)

Figure 9.15: *Two jet event at ZEUS* (a) Side view. (b) Transverse view.

In Sect. 7.4.2 (p. 148) we discussed asymptotic freedom, namely the fact that for $Q^2 \gg \Lambda^2_{\mathrm{QCD}}$ the strong coupling constant $\bar{\alpha}_s \ll 1$. In this case the quarks of the proton are asymptotically free and therefore deep inelastic lepton-proton scattering is not an interaction with the whole proton but with just one of its constituents. This means that coherence and interference are lost (one of mutually exclusive scattering events is taking place) and deep inelastic lepton-proton scattering is an incoherent sum of lepton-quark scattering

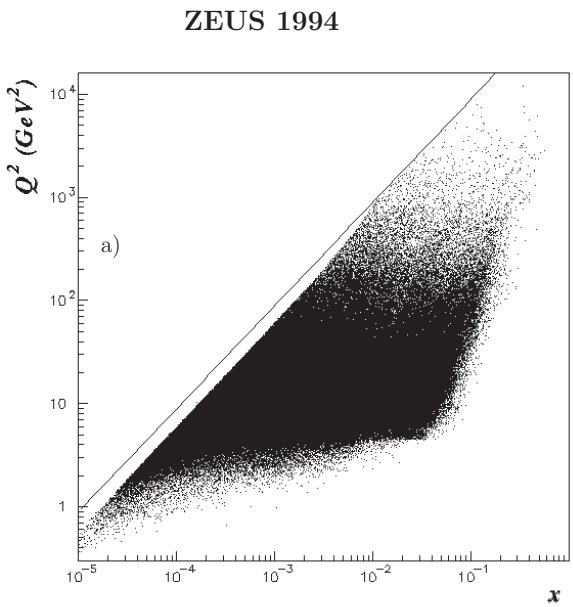

Figure 9.16: Kinematic phase-space measured by the ZEUS experiment.

processes (see Sect. 9.3.2 for diagrams) with the doubly differential cross section[2]

$$\frac{d^2\sigma}{dxdQ^2} = \sum_q \int_0^1 d\xi f_q(\xi) \frac{d^2\hat{\sigma}^{lq}}{dxdQ^2} \tag{9.18}$$

where

- $f_q(\xi)$ is a quark distribution function, i. e. the probability density of finding a quark with momentum ξp inside a proton with momentum p,
- $\xi f_q(\xi)$ is the corresponding momentum density,
- and the hat is used to denote quantities in the lepton-quark system (to distinguish them from lepton-proton system quantities).

Depending on strength and nature of the binding, one expects different behaviors of the momentum density $\xi f_q(\xi)$, as is shown in Fig. 9.19 (compare also Fig. 9.10). If the proton were pointlike the momentum density would be just a delta function, $\delta(1-\xi)$, enforcing $\xi = 1$ for the one particle involved, see Fig. 9.19(a). A proton built out of three *massive* and *weakly coupled* quarks leads to momentum densities consisting of non-ideal delta functions located at $\xi = 1/3$, $1/3\delta(1/3-\xi)$, which are insignificantly smeared out due to the ongoing exchange of binding energy between the quarks with weak, QED like coupling:

[2]Note that ξ and x are not a priori identical. Their relationship under varying assumptions is discussed below and eventually involves QCD corrections.

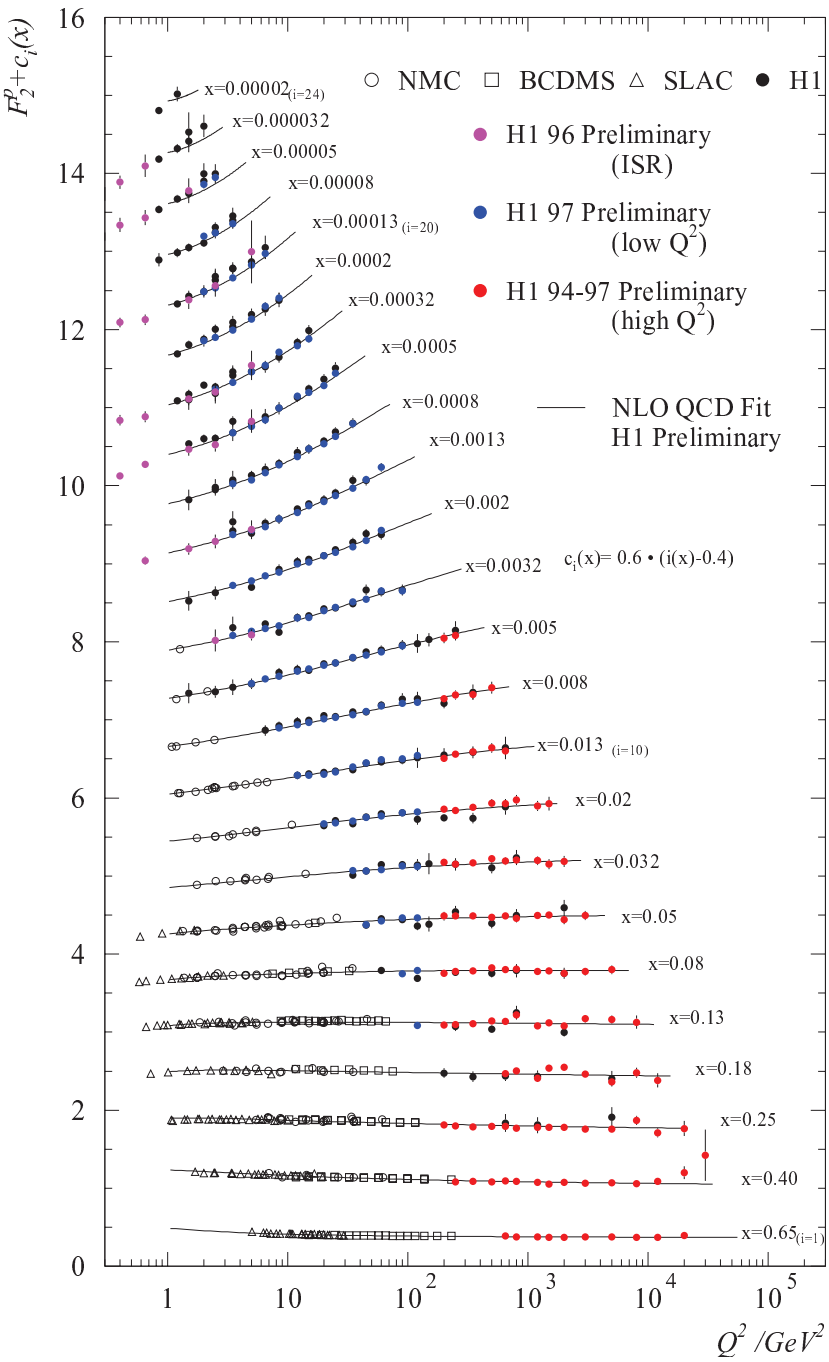

Figure 9.17: Proton structure function F_2^p measured by H1 and other experiments for various values of Q^2 and x. Scaling violations appear for $x < 10^{-2}$.

$m_p \simeq 3m_q$, see Fig. 9.19(b). If, however, the proton consisted of three *light* and *strongly coupled* quarks, $m_q \ll 1/3m_p$, the peaks of $\xi f(\xi)$ would still be located around 1/3, but, since most energy is present in the form of potential and kinetic energy, they would be

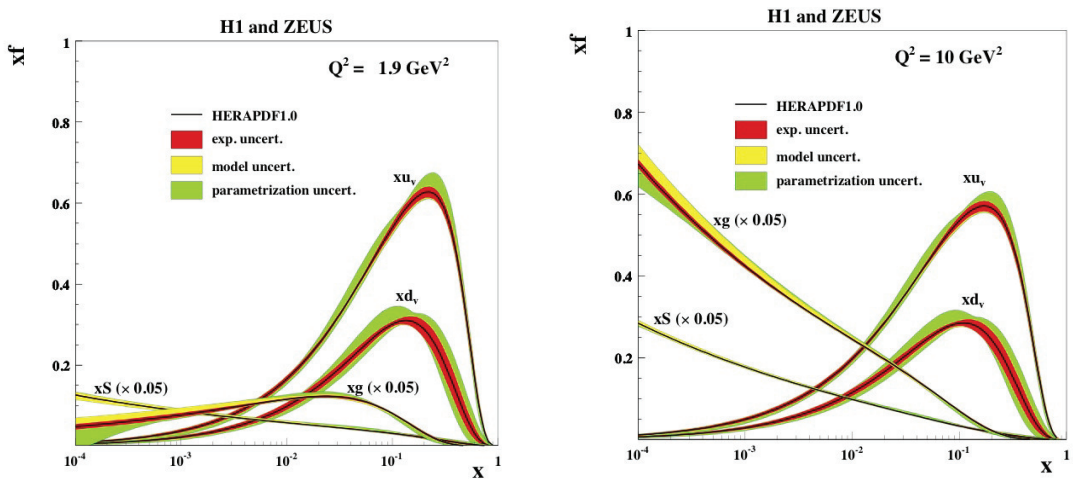

(a) (b)

Figure 9.18: *Parton distribution functions of the proton* (a) $Q^2 = 1.9\,\mathrm{GeV}^2$. (b) $Q^2 = 10\,\mathrm{GeV}^2$. The sea and gluon PDFs are reduced by a factor 20.

smeared out significantly at any given instant of time, as shown in Fig. 9.19(c).

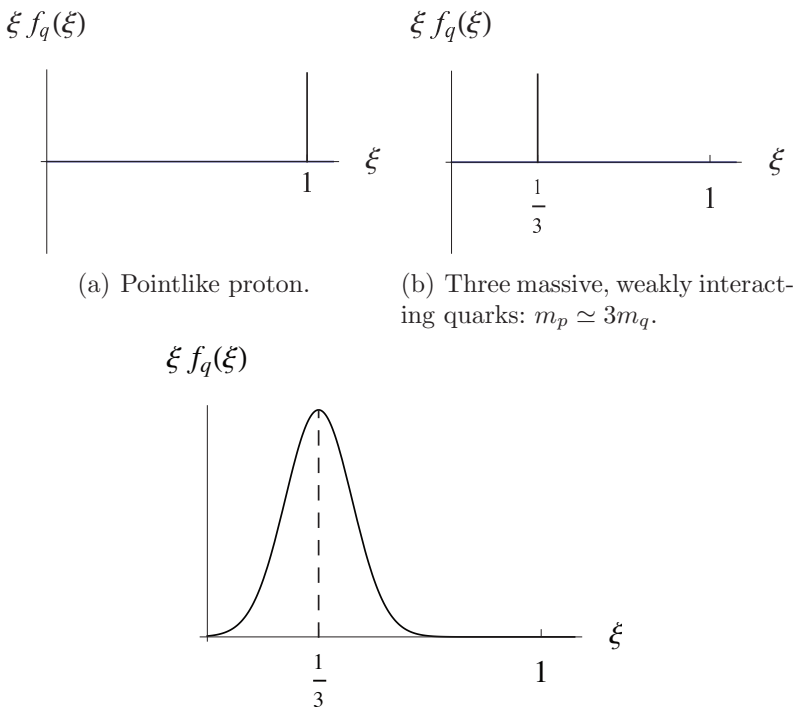

(a) Pointlike proton.

(b) Three massive, weakly interacting quarks: $m_p \simeq 3m_q$.

(c) Three light, strongly coupled quarks: $m_q \ll m_p/3$.

Figure 9.19: *Quark momentum density* $\xi f_q(\xi)$.

Let us consider the kinematics of the simple parton model. The on-shell condition for the outgoing quark (see Fig. 9.20(a)) yields

$$m_q^2 = (\xi p + q)^2 \simeq 2p \cdot q\xi - Q^2 = \frac{Q^2}{x}\xi - Q^2 \Rightarrow \xi = \left(1 + \frac{m_q^2}{Q^2}\right) x \simeq x.$$

Therefore, given the assumptions made are valid, the Bjorken variable x is the momentum fraction ξ of a parton inside the proton.

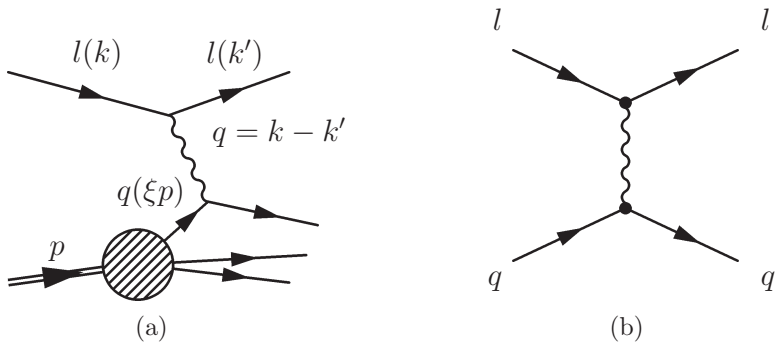

Figure 9.20: *(a) Kinematics of simple parton model and (b) Feynman diagram for lepton-quark scattering.*

To determine $d^2\hat{\sigma}^{lq}/dxdQ^2$ of lepton-quark scattering, we consider the Feynman diagram in Fig. 9.20(b) which is just a crossing of the Born level diagram for $e^+e^- \to \mu^+\mu^-$ (see Sect. 5.10, p. 92). We therefore find

$$\frac{d\hat{\sigma}^{lq}}{dt} = \frac{2\pi\alpha^2 e_q^2}{\hat{s}^2}\left(\frac{\hat{s}^2 + \hat{u}^2}{\hat{t}^2}\right)$$

where the Mandelstam variables read (the subscript ep emphasizes that s_{ep} refers to the lepton-proton system)

$$\begin{aligned}
\hat{s} &= (xp + k)^2 = 2xpk = xs_{ep} \\
\hat{t} &= -Q^2 = -xys_{ep} = t \\
\hat{u} &= -\hat{s} - \hat{t} = -x(1-y)s_{ep}.
\end{aligned}$$

Note that $\hat{t} = t$ depends only on the lepton kinematics. This leads to the lepton-quark differential cross section

$$\frac{d^2\hat{\sigma}^{lq}}{dxdQ^2} = \frac{2\pi\alpha^2 e_q^2}{Q^4}\left(1 + (1-y)^2\right)\delta(x - \xi).$$

Inserting this result into the parton model expression for lepton-proton scattering of Eq. (9.18) yields

$$\frac{d^2\sigma}{dxdQ^2} = \frac{4\pi\alpha^2}{xQ^4}\sum_q \int_0^1 d\xi f_q(\xi) e_q^2 \frac{x}{2}\left(1 + (1-y)^2\right)\delta(x - \xi).$$

Upon comparison with the deep inelastic scattering structure functions we find

$$F_2(x,Q^2) = \sum_q e_q^2 x f_q(x)$$
$$F_L(x,Q^2) = F_2(x,Q^2) - 2xF_1(x,Q^2) = 0$$

where F_L is called longitudinal structure function. We recognize that $F_2(x,Q) = F_2(x)$ ceases to be a function of two variables, but under the assumed conditions depends only on one variable, a phenomenon generally referred to as scaling. Furthermore, $F_L = 0 \Leftrightarrow 2xF_1 = F_2$ is the Callan-Gross relation, a consequence of quarks having spin 1/2 familiar from Sect. 9.3.3.

Before we go on we introduce the following notation for the distribution functions

$$f_q(x) = q(x) \quad (q = u, d, s, c, \dots, \bar{u}, \dots)$$
$$f_g(x) = g(x) \quad (\text{gluons}).$$

9.7 QCD corrections to the parton model

Our discussion of the parton model involved no QCD corrections up to now; it rested on the assumption of electromagnetic interactions alone. QCD corrections will concern the quark part of our diagram. Within the parton model we just found

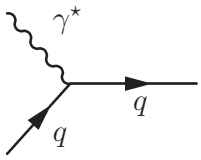

$$= \frac{4\pi\alpha e_q^2}{\hat{s}}\delta(x-\xi) =: \hat{\sigma}_0\delta(x-\xi) \tag{9.19}$$

and

$$\frac{F_2(x,Q^2)}{x} = \sum_q \int_0^1 \frac{d\xi}{\xi} q(\xi) e_q^2\, \delta\left(1 - \frac{x}{\xi}\right) \tag{9.20}$$

where $\hat{\sigma}_0$ is the QED contribution which drops out of the structure functions.

The $\mathcal{O}(\alpha_s) = \mathcal{O}(g_s^2)$ QCD corrections are given by

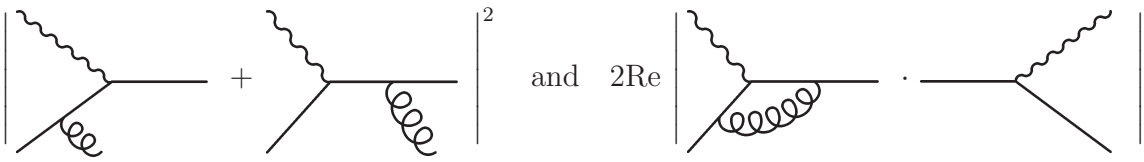

i. e. gluon radiation and virtual gluon exchange. The one-loop virtual gluon interference term stems from the loop corrections to the quark-photon vertex squared at $\mathcal{O}(g_s^2)$. As an example, consider the process $\gamma^\star q \to qg$ (which is a crossing of $\gamma^\star \to q\bar{q}g$):

$$|\mathcal{M}|^2 = 32\pi^2(e_q^2\alpha\alpha_s)C_F\left(-\frac{\hat{t}}{\hat{s}} - \frac{\hat{s}}{\hat{t}} + \frac{2\hat{u}Q^2}{\hat{s}\hat{t}}\right).$$

This expression for $|\mathcal{M}|^2$ is unproblematic for small $\hat{s}$, since $\hat{s}$ is fixed. However, a problem arises at small $\hat{t}$, since we have to integrate over it as it is a dynamic variable (see Sect. 3.3.2, p. 26).

For small scattering angles $-\hat{t} \ll \hat{s}$ and we have

$$p_T^2 = \frac{\hat{s}(-\hat{t})}{\hat{s}+Q^2}$$

for the transverse momentum of the outgoing gluon. Eliminating the Mandelstam variable $\hat{u}$, the differential cross section becomes

$$\frac{d\hat{\sigma}}{dp_T^2} = \frac{1}{16\pi\hat{s}^2}|\mathcal{M}|^2 \simeq \hat{\sigma}_0 \frac{\alpha_s}{2\pi} C_F \left(-\frac{1}{\hat{t}\hat{s}} \left[\hat{s} + \frac{2(\hat{s}+Q^2)Q^2}{\hat{s}} \right] \right).$$

By introducing the dimensionless variable

$$z = \frac{x}{\xi} = \frac{Q^2}{2p_q \cdot q} = \frac{Q^2}{\hat{s}+Q^2},$$

we arrive at

$$\frac{d\hat{\sigma}}{dp_T^2} = \hat{\sigma}_0 \frac{1}{p_T^2} \frac{\alpha_s}{2\pi} P_{qq}(z)$$

where

$$P_{qq}(z) = C_F \frac{1+z^2}{1-z}$$

(compare Sect. 9.4.2). Note that in the simple parton model we had $p_q = \xi p$ which is no longer the case when QCD corrections are taken into account.

To find the inclusive cross section, we have to integrate over the transverse momentum squared:

$$\frac{\hat{\sigma}^{\gamma^\star q \to qg}}{\hat{\sigma}_0} = \frac{\alpha_s}{2\pi} P_{qq}(z) \int_{\mu^2}^{Q^2} \frac{dp_T^2}{p_T^2} = \frac{\alpha_s}{2\pi} P_{qq}(z) \log \frac{Q^2}{\mu^2}$$

where the infrared cutoff μ^2 has been introduced because of the collinear singularity at $p_T^2 \to 0$. The rationale is to later define observables in a way that allows to send $\mu^2 \to 0$ (compare also Sect. 8.2.1, p. 160). Having calculated the QCD corrections at $\mathcal{O}(\alpha_s)$ to the structure function in Eq. (9.20), we can state the resulting corrected expression:

$$\frac{F_2(x,Q^2)}{x} = \sum_q \int_x^1 \frac{d\xi}{\xi} q(\xi) e_q^2 \left\{ \delta\Big(1-\frac{x}{\xi}\Big) + \frac{\alpha_s}{2\pi} \left[P_{qq}\Big(\frac{x}{\xi}\Big) \log \frac{Q^2}{\mu^2} + \text{finite} \right] + \mathcal{O}(\alpha_s^2) \right\} \tag{9.21}$$

which leads to some interesting consequences.[3] Observe that we found an equality of a measurable and hence finite quantity (after all, F_2 is just a specific coefficient in the parametrization of a cross section) and an expression which is divergent at the given order of perturbation theory. Since the LHS of Eq. (9.21) is fixed, the problem has to be tackled on its RHS. As a starting point, recall that we justified the form of the quark distribution functions by asymptotic freedom and neglected QCD interactions among the quarks in the first place. When QCD corrections are taken into account, the naive parton model is no longer valid. Therefore, it is necessary to redefine the parton distribution functions such that they are well-defined for the case of interacting quarks. This amounts to a redefinition of the quark distribution in the infrared region and is called mass factorization of the quark distribution:

$$q(x,\mu_F^2) = q(x) + \frac{\alpha_s}{2\pi}\int_x^1 \frac{d\xi}{\xi} q(\xi) P_{qq}\Big(\frac{x}{\xi}\Big)\log\frac{\mu_F^2}{\mu^2} \tag{9.22}$$

where $q(x,\mu_F^2)$ is a measurable, screened quark density, $q(x)$ denotes the bare (unphysical) quark density, and the integral term is the contribution from unresolvable gluon radiation with transverse momentum $\mu_F^2 \geq p_T^2 \geq \mu^2$ where μ_F^2 is the mass factorization scale at which the quark distribution is measured. Recall that the infrared cutoff μ^2 can be chosen arbitrarily small—smaller than any given detector resolution. At sufficiently small scattering angles the emitted gluon cannot be resolved by the detector as it appears to be parallel to the proton remnants. Two-jet events in deep inelastic scattering can only be excluded in the momentum range where they could be detected. Therefore, the quark distribution $q(x,\mu_F^2)$ admits gluon radiation below a predefined resolution scale μ_F.

Let us solve for $q(x)$ in Eq. (9.22) and plug it into the QCD corrected structure function in Eq. (9.21), we have

$$\begin{aligned}\frac{F_2(x,Q^2)}{x} &= \sum_q \int_x^1 \frac{d\xi}{\xi} q(\xi,\mu_F^2) e_q^2 \left\{ \delta\Big(1-\frac{x}{\xi}\Big) + \frac{\alpha_s}{2\pi} P_{qq}\Big(\frac{x}{\xi}\Big)\log\frac{Q^2}{\mu^2} - \frac{\alpha_s}{2\pi} P_{qq}\Big(\frac{x}{\xi}\Big)\log\frac{\mu_F^2}{\mu^2}\right\} \\ &= \sum_q \int_x^1 \frac{d\xi}{\xi} q(\xi,\mu_F^2) e_q^2 \left\{ \delta\Big(1-\frac{x}{\xi}\Big) + \frac{\alpha_s}{2\pi} P_{qq}\Big(\frac{x}{\xi}\Big)\log\frac{Q^2}{\mu_F^2}\right\}\end{aligned}$$

which is independent of the infrared cutoff μ^2 and finally, setting $\mu_F^2 = Q^2$ as in deep inelastic scattering experiments,

$$= \sum_q q(x,Q^2) e_q^2.$$

Perturbative QCD is used to answer the question how the Q^2 dependence of the quark distribution $q(x,Q^2)$ looks like.

[3] One can observe, as was done before, that because of QCD corrections to the naive parton model scaling no longer holds, since $F_2(x,Q^2)$ ceases to be a function of the single variable x alone.

9.8 Altarelli-Parisi equations

The bare quark distribution $q(x)$ is independent of μ_F^2:

$$\mu_F^2 \frac{d}{d\mu_F^2} q(x) = 0.$$

Differentiating Eq. (9.22) with respect to $\log \mu_F^2$ we thus obtain the renormalization group equation[4] for the quark distribution:

$$\frac{\partial q(x, \mu_F^2)}{\partial \log \mu_F^2} = \frac{\alpha_s}{2\pi} \int_x^1 \frac{d\xi}{\xi} q(\xi, \mu_F^2) P_{qq}\left(\frac{x}{\xi}\right) \tag{9.23}$$

which means that scaling invariance is logarithmically violated.

Eq. (9.23) is known as the **Dokshitzer-Gribov-Lipatov-Altarelli-Parisi** (DGLAP) equation, or simply Altarelli-Parisi evolution equation. It is a small-p_T^2 approximation, which resums the collinear gluon radiation in the initial state at $\mathcal{O}(\alpha_s^n \log^n Q^2)$.

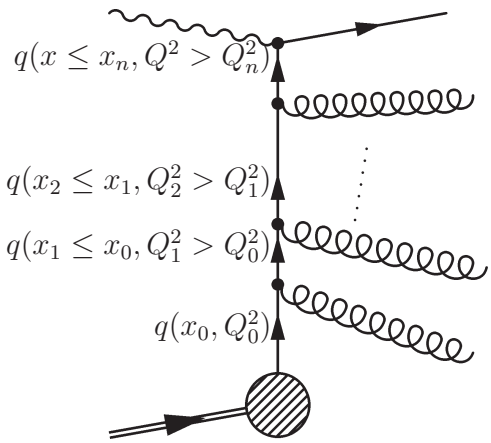

This diagram is a universal correction, since the emitted gluons do not know about the scattering process of the quark off the virtual photon. The DGLAP equation tells us what happens if one infinitesimally increases the resolution. It is an integro-differential equation with one "initial condition" $q(x, \mu_F^2 = \mu_0^2)$. Knowing the latter, one can compute the quark distribution at any value of μ_F^2. The procedure is analogous to the determination of the running coupling of QED (Sect. 6.1.2, p. 102) or QCD (Sect. 7.4.2, p. 148).

In using Eq. (9.23) we omitted until now, the fact that $P_{qq}(z)$ has a singularity in $z = 1$, which belongs to the integration domain. This singularity corresponds to the emitted

[4]For a concise discussion of this topic see [2, pp. 28].

gluon becoming soft. It is compensated by a singularity in the virtual corrections. As a result, $P_{qq}(z)$ is modified to become,

$$P_{qq}(z) = C_F \left(\frac{1+z^2}{(1-z)_+} + \frac{3}{2}\delta(1-z) \right),$$

which takes into account the virtual corrections occuring at $z = 1$. We use the '+'-presciption, coming from the reguarisation procedure and defined by,

$$\int_0^1 dz \frac{f(z)}{(1-z)_+} = \int_0^1 dz \frac{f(z) - f(1)}{1-z}. \tag{9.24}$$

The factor in front of the δ-function can be inferred from the quark number conservation, which can be stated as,

$$\int_0^1 dz P_{qq}(z) = 0. \tag{9.25}$$

Up to now, we considered only gluon radiation off a quark. However, the emission history can be made more complicated with gluons at intermediate stages of the parton cascade,

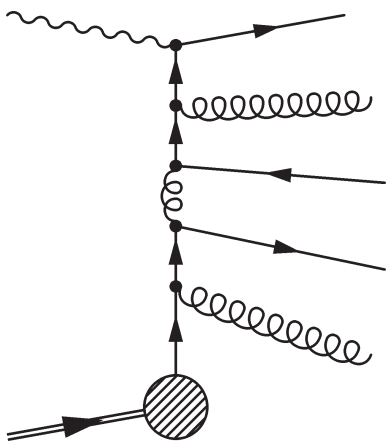

By inspection, one can find out that there are four different splitting processes at $O(\alpha_s)$:

- $q \to q$:

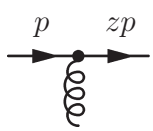

$$\leftrightsquigarrow P_{qq}(z) = C_F \left(\frac{1+z^2}{(1-z)_+} + \frac{3}{2}\delta(1-z) \right), \tag{9.26}$$

- $q \to g$:

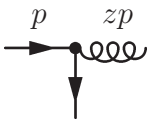

$$\leftrightsquigarrow P_{gq}(z) = C_F \left(\frac{1 + (1-z)^2}{z} \right), \tag{9.27}$$

- $g \to q$:

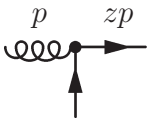

$$\leftrightsquigarrow P_{qg}(z) = T_F \left(z^2 + (1-z)^2 \right), \tag{9.28}$$

- $g \to g$:

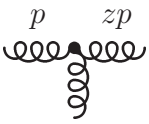

$$\leftrightsquigarrow P_{gg}(z) = 2C_A \left(\frac{z}{(1-z)_+} + \frac{1-z}{z} \right) + \left(\frac{11}{6} C_A - \frac{3}{2} T_F n_f \right) \delta(1-z). \tag{9.29}$$

Those splitting functions satisfy a set of coupled DGLAP equations,

$$\frac{\partial}{\partial \log \mu_F^2} \begin{pmatrix} q(x, \mu_F^2) \\ g(x, \mu_F^2) \end{pmatrix} = \frac{\alpha_s(\mu_F^2)}{2\pi} \int_x^1 \frac{dz}{z} \begin{pmatrix} P_{qq}(z) & P_{qg}(z) \\ P_{gq}(z) & P_{gg}(z) \end{pmatrix} \begin{pmatrix} q\left(\frac{x}{z}, \mu_F^2\right) \\ g\left(\frac{x}{z}, \mu_F^2\right) \end{pmatrix}. \tag{9.30}$$

In this equation, $\frac{\alpha_s}{2\pi} P_{ji}(z)$ is the probability for $i \to j$ splitting with momentum fraction z in the transverse momentum interval $[\log \mu_F^2, \log \mu_F^2 + d \log \mu_F^2]$.

For n_f quark flavours, we get $2n_f + 1$ coupled equations (antiquarks must be taken explicitly into account). This system can be diagonalized be introducing (i labels the flavour),

- n_f valence quark distributions

$$q_i^V = q_i - \bar{q}_i, \tag{9.31}$$

- $n_f - 1$ flavour non-singlet quark distributions

$$q_i^F = \sum_{n=1}^{i-1} (q_n + \bar{q}_n - q_i - \bar{q}_i), \tag{9.32}$$

- 1 flavour singlet quark distribution

$$q^S = \sum_{n=1}^{n_f} (q_n + \bar{q}_n). \tag{9.33}$$

We also define the convolution,

$$(P \otimes q)(x, \mu_F^2) = \int_x^1 \frac{dz}{z} P(z) q\left(\frac{x}{z}, \mu_F^2\right),$$

allowing us to write,

$$\frac{\partial q_i^V}{\partial \log \mu_F^2} = \frac{\alpha_s}{2\pi} P_{qq} \otimes q_i^V \tag{9.34}$$

$$\frac{\partial q_i^F}{\partial \log \mu_F^2} = \frac{\alpha_s}{2\pi} P_{qq} \otimes q_i^F \tag{9.35}$$

$$\frac{\partial q^S}{\partial \log \mu_F^2} = \frac{\alpha_s}{2\pi} \left(P_{qq} \otimes q^S + 2n_f P_{qg} \otimes g\right) \tag{9.36}$$

$$\frac{\partial g}{\partial \log \mu_F^2} = \frac{\alpha_s}{2\pi} \left(P_{gq} \otimes q^S + P_{gg} \otimes g\right). \tag{9.37}$$

The factor $2n_f$ in Eq. (9.36) comes from the fact that one needs to consider quarks and antiquarks of all possible flavours. This set of equations only includes leading order corrections that are precise at 15%. The data obtained in the last years yield however results to the 5% precision, so that correction from higher orders need to be taken into account.

At NLO, $\mathcal{O}(\alpha_s^n \log^{n-1} Q^2)$, the finite term from the $\mathcal{O}(\alpha_s)$-processes is relevant,

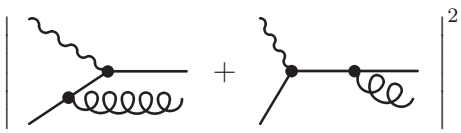

This translates in the expressions for the structure functions,

$$\frac{1}{x} F_2(x, Q^2) = \int_x^1 \frac{d\xi}{\xi} \left\{ \sum_q q\left(\xi, Q^2\right) \left[\delta\left(1 - \frac{x}{\xi}\right) + \frac{\alpha_s}{2\pi} C_{2,q}\left(\frac{x}{\xi}\right)\right] + g(\xi, Q^2) \frac{\alpha_s}{2\pi} C_{2,g}\left(\frac{x}{\xi}\right) \right\} \tag{9.38}$$

$$F_L(x, Q^2) = \mathcal{O}(\alpha_s) \neq 0 \tag{9.39}$$

We now need to compute $O(\alpha_s^2)$-corrections to the spitting functions P_{ji}. At this order, there is essentially one new spitting process with two quark-gluon vertices,

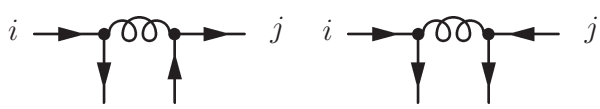

At $O(\alpha_s)$, we had implicitly $P_{qq}^V = P_{qq}^F = P_{qq}^S = P_{qq}$ in Eqs. (9.34), (9.35) and (9.36). This is no longer true at $O(\alpha_s^2)$, where all these splitting functions are different from one another. At even higher orders, no essentially new features appear, so that NLO calculations lead already quite acceptable results. These are of crucial importance for W and Z production at hadron colliders.

9.9 Solution of DGLAP equations

Looking at the set (9.30) of coupled DGLAP integro-differential equations one can expect that solving it could be a highly non-trivial task. There are basically two approaches to attack the problem :

1. Numerical solution, e.g. with the Runge-Kutta method. This approach is yielding satisfactory results for $Q_0^2 \gtrsim 2\,\mathrm{GeV}$, i.e. in the asymptotically free regime, where $\alpha_s(Q_0^2) \ll 1$,

2. Analytically, by using Mellin tranformation. This approach is especially useful to obtain a quantitative understanding and to determine the asymptotic properties.

In both cases we have to start from given initial distributions $q_i(x, Q_0^2), \bar{q}_i(x, Q_0^2), g(x, Q_0^2)$.

Mellin transformation The Mellin transform of a function $f : [0, 1] \to \mathbb{R}$ is given by,

$$f(n) = M[f(x)] = \int_0^1 dx x^{n-1} f(x), \tag{9.40}$$

with inverse

$$f(x) = \frac{1}{2\pi i} \int_{a-i\infty}^{a+i\infty} dn x^{-n} f(n), \tag{9.41}$$

for $f(n)$ analytical in the half plane $\mathrm{Re}\, n > a$.

We list here some of the properties of Mellin transformations:

$$M[af(x) + bg(x)] = af(n) + bg(n) \qquad \text{(linearity)} \tag{9.42}$$

$$M\left[\frac{d^k}{dx^k} f(x)\right] = (-1)^{n-k} \frac{\Gamma(n)}{\Gamma(n-k)} f(n-k) \qquad \text{(derivative)} \tag{9.43}$$

$$M[(f \otimes g)(x)] = f(n)g(n) \qquad \text{(convolution)} \tag{9.44}$$

Armed with this new technology, we Mellin transform Eq. (9.34) with respect to the x variable to get (the following analysis is valid for the valence and flavour non-singlet quark distribution, thus, we drop the i, V/F for notational convenience),

$$\frac{\partial q(n,\mu_F^2)}{\partial \log \mu_F^2} = \frac{\alpha_s(\mu_F^2)}{2\pi} P_{qq}(n) q(n,\mu_F^2). \tag{9.45}$$

Using the evolution equation for α_s (Sect. 7.4.2, p. 151) in the leading order approximation,

$$\frac{1}{\alpha_s}\frac{\partial \alpha_s}{\partial \log \mu_F^2} = \frac{\partial \log \alpha_s}{\partial \log \mu_F^2} = -\frac{\beta_0}{4\pi}\alpha_s,$$

one gets,

$$\begin{aligned} \frac{\partial q(n,\mu_F^2)}{\partial \log \alpha_s} &= -\frac{2}{\beta_0} P_{qq}(n) q(n,\mu_F^2) \\ \frac{\partial \log q(n,\mu_F^2)}{\partial \log \alpha_s} &= -\frac{2}{\beta_0} P_{qq}(n), \end{aligned} \tag{9.46}$$

which can now be solved by integrating from $\mu_F^2 = Q_0^2$ to Q^2,

$$q(n,Q^2) = q(n,Q_0^2)\left[\frac{\alpha_s(Q_0^2)}{\alpha_s(Q^2)}\right]^{\frac{2}{\beta_0}P_{qq}(n)},$$

or, in the usually known form, using Eq. (7.44), p. 152,

$$\boxed{q(n,Q^2) = q(n,Q_0^2)\exp\left\{\frac{2}{\beta_0}P_{qq}(n)\log\frac{\log(Q^2/\Lambda^2)}{\log(Q_0^2/\Lambda^2)}\right\}}. \tag{9.47}$$

This is the solution for the quark valence and flavour non-singlet distributions.

We now turn to the two remaining distributions, namely the quark singlet and and gluon distributions. Mellin transforming Eqs. (9.36) and (9.37) yields,

$$\frac{\partial}{\partial \log \mu_F^2}\begin{pmatrix} q^S(n,\mu_F^2) \\ g(n,\mu_F^2) \end{pmatrix} = -\frac{2}{\beta_0}\begin{pmatrix} P_{qq}(n) & 2n_f P_{qg}(n) \\ P_{gq}(n) & P_{gg}(n) \end{pmatrix}\begin{pmatrix} q^S(n,\mu_F^2) \\ g(n,\mu_F^2) \end{pmatrix}. \tag{9.48}$$

The first step is the diagonalization of the matrix,

$$\begin{pmatrix} P_{qq}(n) & 2n_f P_{qg}(n) \\ P_{gq}(n) & P_{gg}(n) \end{pmatrix}.$$

Then one applies the same formalism as for the valence quark distribution discussed above. By inverse Mellin transformation, one gets the result in the variable x.

Specific values of n correspond to various physical quantities. For example, $P_{qq}(n=1) = 0$ is the Mellin transform of Eq. (9.25) and $q(n=2)$ corresponds to the fraction of the total momentum transported by the quark q. One has the momentum sum rule,

$$q^S(2,Q^2) + g(2,Q^2) = 1.$$

with the asymptotic values,

$$q^S(2, Q^2 \to \infty) \to \frac{3n_f}{16 + 3n_f} \overset{n_f=5}{=} \frac{15}{31}$$
$$g(2, Q^2 \to \infty) \to \frac{16}{16 + 3n_f} \overset{n_f=5}{=} \frac{16}{31}.$$

9.10 Observables at hadron colliders

We now study processes and observables at hadron colliders and the consequences of parton evolution in this context.

The simple parton model cross section for processes at hadron-hadron colliders reads

$$\sigma_{pp} = \sum_{i,j \in \{q,g\}} \int dx_1 dx_2 f_i(x_1) f_j(x_2) \hat{\sigma}_{ij \to X}(s_{ij} = x_1 x_2 s_{pp}), \tag{9.49}$$

i. e. two partons enter into a hard collision from which a final state X emerges, as shown in Fig. 9.21(a).

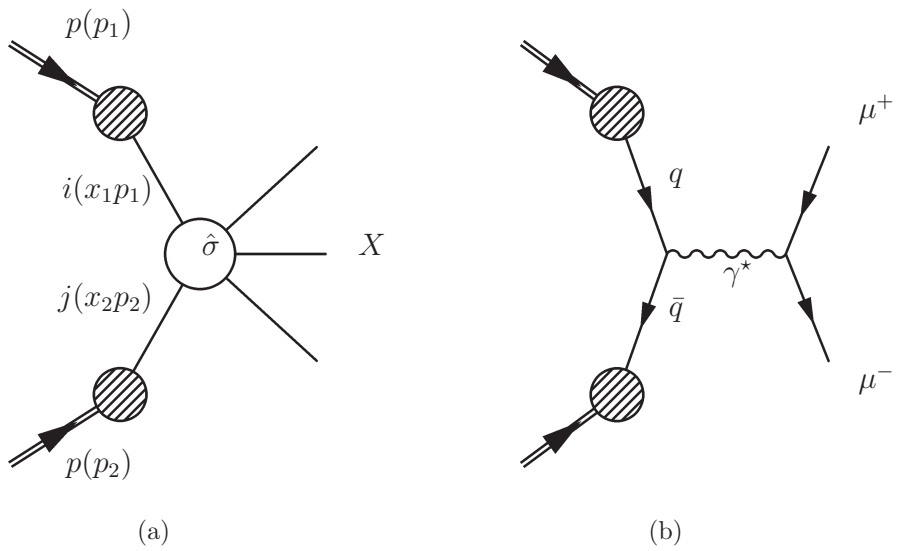

Figure 9.21: *(a) Hadron-hadron collision in naive parton model and (b) Drell-Yan process.*

As an example consider the Drell-Yan process, $pp \to \mu^+\mu^-$, shown in Fig. 9.21(b). The parton model cross section reads

$$\sigma^{\mathrm{DY}} = \sum_q \int dx_1 dx_2 \left[q(x_1)\bar{q}(x_2) + q(x_2)\bar{q}(x_1) \right] \hat{\sigma}_{q\bar{q} \to \mu^+\mu^-} \tag{9.50}$$

where

$$\hat{\sigma}_{q\bar{q}\to\mu^+\mu^-} = \underbrace{\frac{4\pi\alpha^2}{3s_{q\bar{q}}}\frac{1}{3}}_{\hat{\sigma}_0^{\mathrm{DY}}} e_q^2\,\delta(1 - x_1x_2s_{pp}/M^2_{\mu^+\mu^-}) \tag{9.51}$$

which we basically already calculated before (Sect. 5.10, p. 92). The difference to the $e^+e^- \to \mu^+\mu^-$ result is the color factor of 1/3 and the delta function which states that the muon pair invariant mass fulfills $(p_{\mu^+} + p_{\mu^-})^2 =: M^2_{\mu^+\mu^-} = x_1x_2s_{pp}$.

The following QCD corrections have to be included:

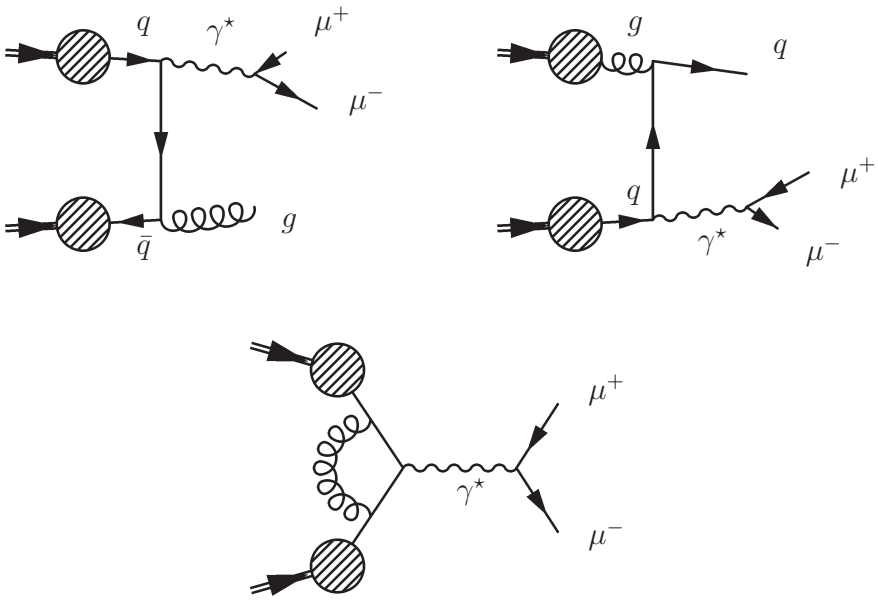

where the first two diagrams are because of parton evolution and the third diagram is a virtual correction. Setting $z = x_1x_2s_{pp}/M^2_{\mu^+\mu^-}$, the QCD corrected Drell-Yan cross section reads

$$\sigma^{\mathrm{DY}} = \hat{\sigma}_0^{\mathrm{DY}} \sum_q e_q^2 \int dx_1 dx_2 \Big\{ q(x_1)\bar{q}(x_2)\delta(1-z) + \frac{\alpha_s}{2\pi} C_{q\bar{q}}(z) \\ + [q(x_1) + \bar{q}(x_1)]\, g(x_2) \frac{\alpha_s}{2\pi} C_{qg}(z) + (x_1 \leftrightarrow x_2) \Big\}$$

where $q(x_i)$ etc. are the QCD evolved parton distributions.

In the following some standard reactions are listed.

- $W^\pm$, Z^0 *production*

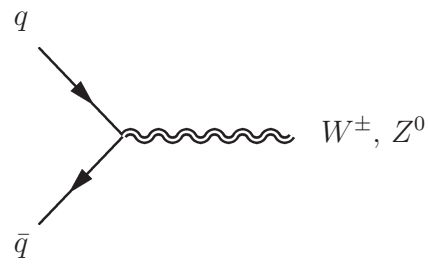

- $\gamma +$ jet *production*

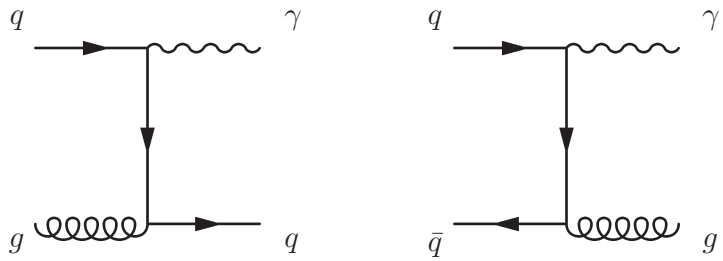

- *2-jet production*

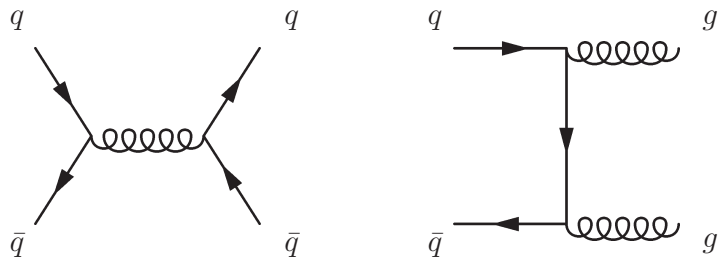

Further processes leading to 2-jet events are $qg \to qg$, $gg \to gg$, $gg \to q\bar{q}$ and $qq \to qq$.

Examples for relevant processes in searches for new physics:

- *Higgs production*

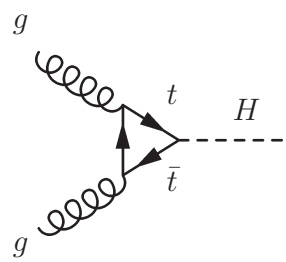

- *SUSY particles*

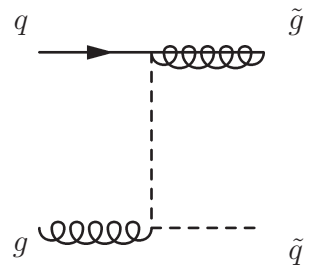

A general feature of hadron-hadron colliders is that $\sqrt{s_{\text{parton-parton}}}$ is variable since the parton momentum fractions vary.[5] This allows to search for peaks in mass spectra at fixed collider energy. An example for this effect is the Z^0 peak in the $\mu^+\mu^-$ spectrum of SPS at CERN (compare also Sect. 4.4.4, p. 51).

9.11 Multiparticle production

Describing multijet final states in QCD is problematic because of two reasons.

- *Factorial growth of the number of diagrams*
  E. g. for $gg \to ng$ the number of diagrams # scales with the number of final state gluons n in the following way:

n	2	3	4	5	6	7
#	4	25	220	2485	34300	559405.

  These numbers illustrate that a computation even on the amplitude level is time-consuming.

- *Complexity of the final state phase space*
  In addition to the aforementioned problem, the final state phase space has high dimension and the integrations are constrained in various ways.

These problems can be approached by introducing approximate descriptions. One uses the fact that $|\mathcal{M}|^2$ is largest if partons are emitted into soft ($E \to 0$) or collinear ($\theta_{ij} \to 0$) regions of phase space. Therefore, the dominant contributions stem from these phase space regions.

[5] Compare this to the e^+e^- case where the center of mass energy of the actual collision is fixed by the collider energy: $s = \hat{s}$.

Let us analyze a collinear parton shower. Consider the shower subgraph

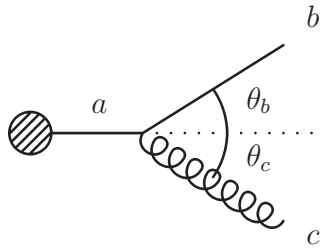

where $p_a^2 \gg p_b^2, p_c^2$ and $p_a^2 = t$. The opening angle is $\theta = \theta_b + \theta_c$ and the energy fractions are

$$z = \frac{E_b}{E_a} \qquad\qquad 1 - z = \frac{E_c}{E_a}. \tag{9.52}$$

For small angles we have

$$t = 2E_b E_c(1 - \cos\theta) = z(1-z)E_a^2\theta^2 \tag{9.53}$$

$$\frac{\theta_b}{1-z} = \frac{\theta_c}{z} = \theta. \tag{9.54}$$

For $\theta \to 0$ the matrixelement factorizes as

$$|\mathcal{M}_{n+1}|^2 = \frac{4g_s^2}{t} C_F F_{qq}(z) |\mathcal{M}_n|^2$$

where

$$F_{qq}(z) = \frac{1+z^2}{1-z} = P_{qq}(z < 1).$$

Analogous splittings involve F_{qg}, F_{gq}, and F_{gg}.

Also the phase space factorizes:

$$d\phi_n = \ldots \frac{d^3p_a}{2E_a(2\pi)^3}$$

$$d\phi_{n+1} = \ldots \frac{d^3p_b}{2E_b(2\pi)^3} \frac{d^3p_c}{2E_c(2\pi)^3}.$$

Since $p_c = p_a - p_b$, we have $d^3p_c = d^3p_a$ for fixed p_b. For small θ this yields[6]

$$\begin{aligned} d\phi_{n+1} &= d\phi_n \frac{1}{2(2\pi)^3} \int E_b dE_b \theta_b d\theta_b d\phi \frac{dz}{1-z} \delta(z - E_b/E_a) dt \delta(t - E_a E_b \theta^2) \\ &= d\phi_n \frac{1}{4(2\pi)^3} dt dz d\phi \end{aligned}$$

(recall Eq. (9.52) and (9.53)).

Since the matrixelement and the phase space factorize, so does the cross section:

$$d\sigma_{n+1} = d\sigma_n \frac{dt}{t} dz \frac{d\phi}{2\pi} \frac{\alpha_s}{2\pi} C_F F(z).$$

Therefore, multiple emission processes like

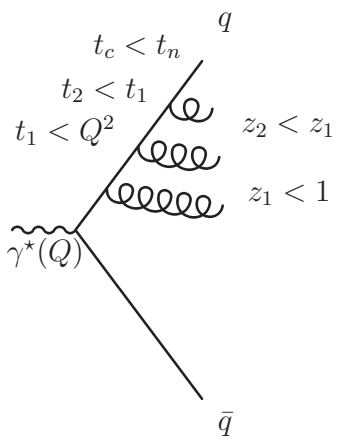

where t_c is a cutoff scale at which hadronization sets in, $t_c \gtrsim \Lambda^2_{\mathrm{QCD}}$, can be subdivided into fundamental steps in (t, z) space:

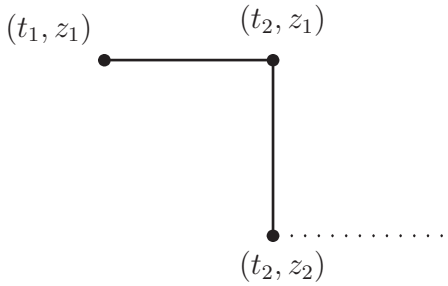

A Monte Carlo method to generate a corresponding set of final state partons proceeds as

[6] One observes that

$$\begin{aligned} d\phi_{n+1} &= \cdots \frac{d^3p_b}{2E_b(2\pi)^3} \frac{d^3p_c}{2E_c(2\pi)^3} = d\phi_n \frac{E_a}{E_c} \frac{d^3p_b}{(2\pi)^3 2E_b} \\ &\simeq d\phi_n \frac{E_a}{E_c} \frac{E_b dE_b}{2(2\pi)^3} \theta_b d\theta_b d\phi = d\phi_n \frac{1}{1-z} \frac{E_b dE_b}{2(2\pi)^3} \theta_b d\theta_b d\phi. \end{aligned}$$

And the Jacobian determinant is just $2zE_a\theta_b/(1-z)$.

follows: Starting from a simple final state (e. g. $e^+e^- \to q\bar{q}$), generate additional partons step-by-step while admitting only visible (i. e. non-soft) emission:

$$z > \varepsilon(t) \qquad\qquad (1-z) > \varepsilon(t)$$

where $\varepsilon(t)$ can be expressed in the following way:

$$\begin{aligned}
&p_a^2 = t \text{ and } p_b^2, p_c^2 > t_c \\
&p_T^2 = z(1-z)p_a^2 - (1-z)p_b^2 - zp_c^2 > 0 \\
&\Rightarrow z(1-z) > \frac{t_c}{t} \\
&\Rightarrow \varepsilon(t) = \frac{1}{2} - \frac{1}{2}\sqrt{1 - 4\frac{t_c}{t}} \simeq \frac{t_c}{t}
\end{aligned}$$

which means that the threshold $\varepsilon(t)$ gets more strict for decreasing t.

Let us define the Sudakov form factor $\Delta(t)$

$$\Delta(t) = \exp\left\{ -\int_{t_c}^{t} \frac{dt'}{t'} \int_{\varepsilon(t')}^{1-\varepsilon(t')} dz \alpha_s C_F F_{qq}(z) \right\}$$

which is the probability for a parton to evolve from t to t_c without emission of another parton. Observe that

$$\Delta(t_c) = 1$$

and the probability for a parton to evolve from $t_1 \to t_2$ without emission of another parton is given by

$$R(t_1, t_2) = \frac{\Delta(t_1)}{\Delta(t_2)}.$$

The Monte Carlo procedure is now as follows.

0. Starting point (t_1, z_1)
1. Generate a random number $R \in]0;1[$.
2. Solve $\Delta(t_1)/\Delta(t_2) = R$ for t_2.
   - For $\Delta(t_1) > R$:
     $\Delta(t_2) > 1$: $t_2 < t_c$: no emission, parton saved for final state

- For $\Delta(t_1) < R$:
  Generate further random number $R' \in]0;1[$ and solve

$$\int_{\varepsilon(t_2)}^{z_2/z_1} dz \frac{\alpha_s}{2\pi} P(z) = R' \int_{\varepsilon(t_2)}^{1-\varepsilon(t_2)} dz \frac{\alpha_s}{2\pi} F(z)$$

  for z_2.

3. Use the two new partons

$$\left((t_2, z_2); \left(t_2, \frac{z_1 - z_2}{z_1}\right)\right)$$

   as starting point for another Monte Carlo step (see Fig. 9.22).

4. Repeat steps 1 to 3 until all partons fulfill $t_i < t_c$.

This procedure generates events with the same probabilities as in experiment and produces a list of final state particles which allows to perform the same analyses as on experimental data. This is how one arrives at the "theory curves" shown e. g. in some of the plots in Chap. 8.

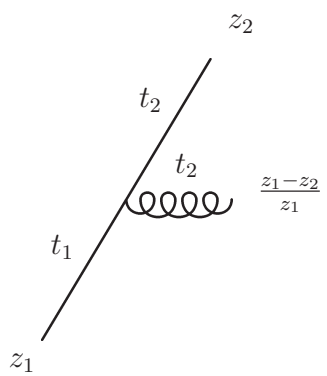

Figure 9.22: *Starting point for second Monte Carlo step.*